Spitzer IRS data on λ Boötis stars: debris disks or diffuse ISM dust ?

Marlies Spijkman

Kapteyn Astronomical Institute, University of Groningen, Groningen, the Netherlands

Report Klein Onderzoek

supervisor: dr. I. Kamp

Groningen, June 2012

Cover figure.

Zeta Ophiuchi, a runaway star plowing through space dust. The blue star near the center of this image is Zeta Ophiuchi. When seen in visible light it appears as a relatively dim red star surrounded by other dim stars and no dust. However, in this infrared image taken with NASA's WISE telescope, a completely different view emerges. Zeta Ophiuchi is actually a very massive, hot, bright blue star plowing its way through a large cloud of interstellar dust and gas. While somewhat different than λ Boötis stars, current ideas suggest that their properties may be understood as a result of them plowing their way through surrounding gas and dust. Image copyright: NASA/JPL-Caltech/UCLA.

Spitzer IRS data on λ Boötis stars: debris disks or diffuse ISM dust?

M. Spijkman

supervisor: Dr. I. Kamp

July 10, 2012

Abstract

λ Boötis stars are late-B to early-F type stars that are known to have a peculiar chemical abundance pattern. While they have roughly solar abundances of light elements (C, N, O, and S), the Fe-peak elements are significantly depleted. The abundance pattern of λ Boötis stars may be physically connected to their infrared (IR) excess.

We investigate the circumstellar environment of a sample of λ Boötis stars in an effort to distinguish between different scenarios. If a debris disk gives rise to the infrared excess, the λ Boötis phenomenon may be related to the properties and evolution of the disk and be circumstellar in origin. On the other hand, if the anomalous abundance pattern is a result of selective accretion of interstellar gas, the infrared excess may be caused by an interstellar reflection nebula. SED modeling alone is not sufficient to constrain the properties of the stellar environment. Therefore we have performed a spectroscopic study with Spitzer IRS data to analyze the composition of the surrounding material of λ Boötis stars. This analysis also included a search for PAH features, since they would be a clear indication of the presence of interstellar matter.

One of the conclusions of our project is that no signatures of PAHs could be detected in the IRS spectra. On the other hand, we have found that the onset of the infrared excess seems to indicate the presence of small sized grains. This implicates an interstellar origin of these grains, which may be an indication for the accretion of interstellar matter onto the stars. However, conclusive evidence has not been found.

1 Introduction

The observed surface composition of many stars can be understood to a satisfactory level with our current understanding of stellar evolution. It accurately predicts the interior gas dynamics and chemical composition for different types of stars at any stage in their life. Stellar spectra reveal the surface composition of stars, which is often comparable to the predicted surface composition from the stellar models. The spectrum of our own Sun is also frequently used as a reference for the average composition of Population I stars.

But some stars still fall outside the box. Their surface composition is drastically different than expected, considering their generation and size. λ Boötis stars are such outcasts, characterized by a considerable lack of heavier elements at their surface, which cannot be explained within the present theory of stellar evolution. None of the theories for this anomaly has been generally accepted yet. Understanding the mechanism of the λ Boötis phonomenon is essential for a complete theory of stellar structure and evolution, and the extent and manner in which these are influenced by the stellar surroundings.

We will first give a quick overview of the historic development of the research in λ Boötis stars and related types of stars, compare the competing theories for the λ Boötis phenomenon and place the goal of the present research into context.

1.1 History and definition of λ Boötis stars

The prototype for the class of λ Boötis stars is the star λ Boo in the constellation Boötes. Its peculiarity was first noted by Morgan, Keenan and Kellman, who described the spectral characteristics of λ Boo that set it apart from 'normal' A-stars in their atlas of stellar spectra of 1943 [17]. Two more stars with similar spectral features, ^{29}Cyg (HD192640) and π^1Ori (HD31295), were identified in the 1950s by Slettebak (1952, 1954) [22, 23]. He found that most metallic lines in the spectra of λ Boo, ^{29}Cyg and π^1Ori were considerably weakened relative to a normal star of the same spectral type and consequently identified them as 'weak-line stars'. Burbidge & Burbidge (1956) [2] were the first to analyze the abundances of a sample of weak-line stars quantitatively. Gray (1988) [7] proposed the first working definition for λ Boötis stars, mainly derived from their spectroscopic characteristics. It may be summarized as follows [18]:

- λ Boötis stars are classified as late-B to early-F type stars based on their hydrogen lines.
- Their broad hydrogen lines and space velocity indicate that they are Population I stars.
- They have solar surface abundances of light elements (C, N, O and S).
- They are generally metal-weak with underabundances of Fe-peak elements up to a factor of 100.

Less than 2% of all stars in the relevant spectral region satisfies the λ Boötis definition, which indicates either uncommon conditions or a short-lived phenomenon. Furthermore,

Figure 1: The Boötis constellation in the Northern sky, as portrayed in Urania's Mirror, a set of 32 constellation cards published in London in 1825 AD. The name comes from the Greek Βοώτης, meaning 'herdsman'. He follows Ursa Major around the North pole with his two hunting dogs, Canes Venatici (thus keeping the heavens in constant rotation according to some myths). Below them is the constellation of Coma Berenices, and above them is Quadrans Muralis, now obsolete. λ Boötis, the prototype for λ Boötis stars, is located in the upper arm of the herdsman in the picture. [28]

the λ Boötis pattern is found continuously from the zero-age main sequence to the terminal-age main sequence. Fig. 2 shows the mean abundance pattern for a selection of 34 λ Boötis stars by Heiter (2002) [8]. The largest and smallest occurring abundances are also shown. The λ Boötis pattern is clearly visible in the mean abundances, with depleted heavy elements and nearly solar light elements. However, the minimum and maximum observed abundances in the sample indicate a large variation in the abundances among the different λ Boötis stars. The abundance ranges in λ Boötis stars are also significantly larger for almost all elements than for normal stars in the Hyades open cluster and stars in the galactic field. This indicates that even though the λ Boötis abundance pattern is very characteristic, the group as a whole is rather inhomogeneous. Any theory explaining the λ Boötis phenomenon needs to explain these large variations as well.

Gray (1988) [7] composed a list of probable λ Boötis candidates on the basis of the above definition. This list has steadily evolved to that of Paunzen et al (2002) [19], which is the master list from which the sample of stars for this study has been selected.

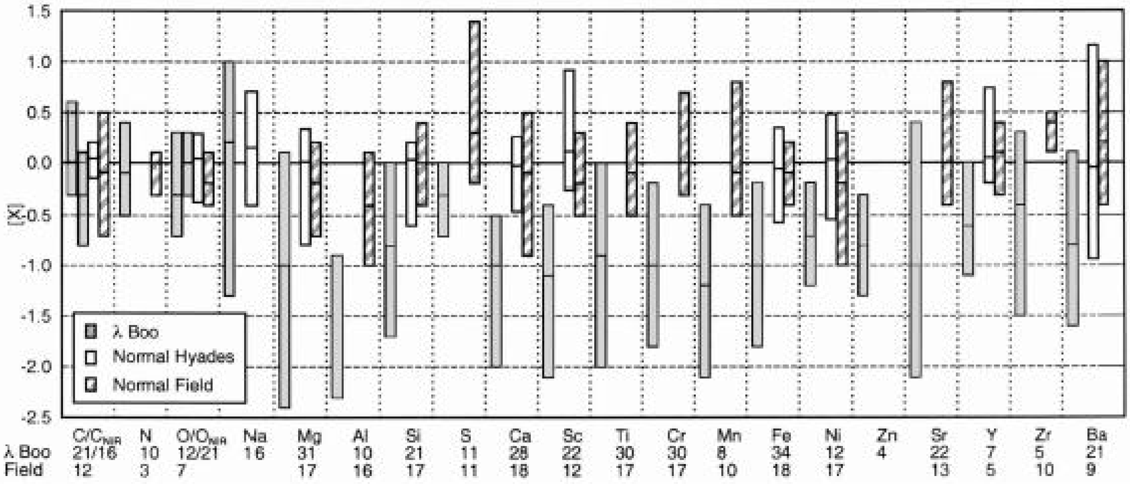

Figure 2: Mean abundances relative to the Sun taken from the literature of a sample of 34 λ Boötis stars (middle lines in grey bars), as well as highest and lowest abundances (upper and lower limit of bars). The same for normal stars in the Hyades open cluster (white bars) as well as normal field stars (hashed bars). The C and O abundances for λ Boötis stars have been determined from both optical and near infrared (NIR) spectra. The number of available abundances in the literature for the λ Boötis and field stars is given below the element name. [8]

1.2 Peculiar stars

All λ Boötis stars are late B- to early F- type stars, based on their hydrogen lines. Many stars that are classified within this spectral range appear to have unusual surface abundances and are thus referred to as peculiar stars. In particular the abundances of elements around the Fe-peak can differ from our initial expectations by as much as 2 orders of magnitude. But they do share a common feature that supports the potential development of any surface anomalies. All these stars have no surface convection zones or only very thin ones that are inefficient in mixing material over large vertical distances.

Convection zones arise when temperature instabilities develop between layers of gas. The temperature of a star decreases from its center outwards. A rising bubble of gas adjusts itself to the lower gas pressure and expands. It will hardly have time to interact with its new environment and will therefore cool primarily by adiabatic expansion. When the gas bubble has not cooled as much as its surroundings by the time it has reached a pressure equilibrium, it will be less dense than the surroundings and it will be accelerated upwards by the buoyancy force. As long as the bubble is unable to cool sufficiently to reach a temperature equilibrium it will continue to rise and a falling bubble of gas will continue to fall due to the reverse mechanism. Layers of gas thus become unstable if the temperature gradient is much steeper than the internal temperature adjustments by adiabatic expansion of moving bubbles of gas.

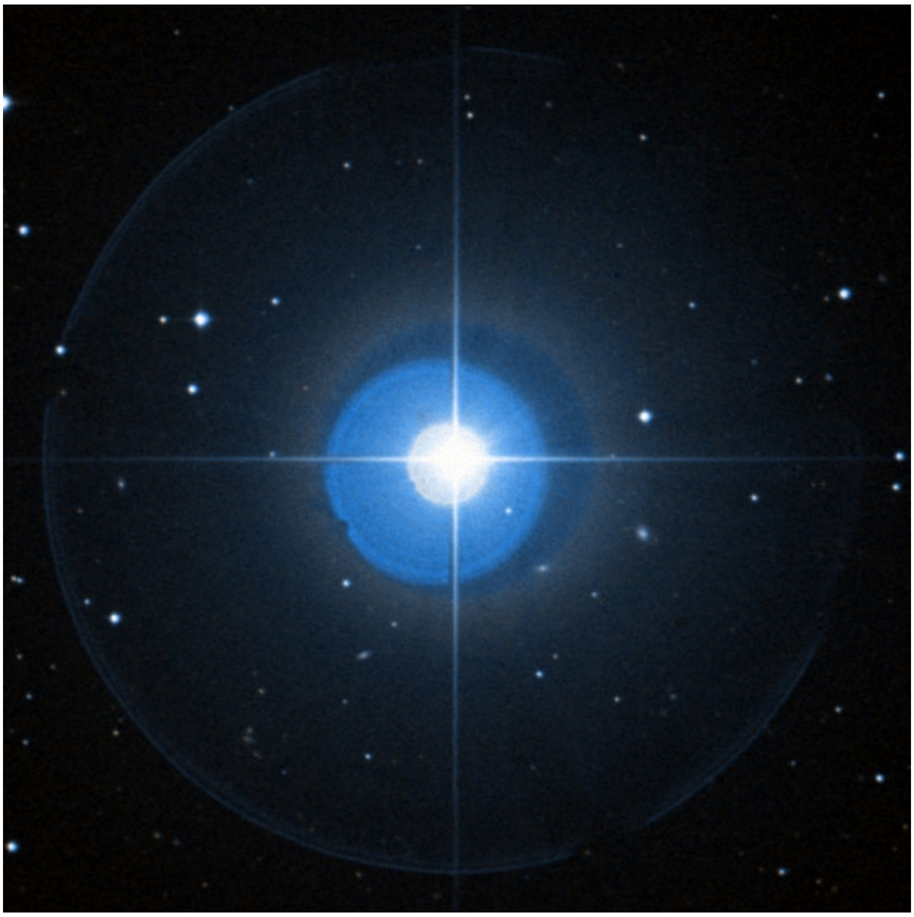

Figure 3: Image of λ Boötis, the prototype for λ Boötis stars. Courtesy of Centre de Données Astronomiques de Strasbourg.

The temperature gradient can become very steep if not all energy is used to heat the gas, for example when many particles go through a phase transition or become ionized while they are heated. The most abundant elements in the surface of stars are hydrogen and helium, and their ionization can cause abrupt temperature differences in the stellar surface layers. But the effective temperature of late B- to early F- type stars is so high, that all or most hydrogen is ionized at the surface, and it is not or hardly high enough to ionize helium. Therefore the surface temperature gradient is small and they either have no surface convection zone or only very shallow and inefficient ones. Superficial deviations can then develop either by particular surface conditions or by an external influence and will be sustained for a long period of time. The various peculiarities that are observed among these stars may thus have very different causes. We discuss the possible causes for λ Boötis stars in the following sections.

1.3 Competing theories

In this subsection we provide a short overview of the three main competing theories for the λ Boötis phenomenon. The selective accretion theory is the theory that is investigated in this project.

1.3.1 Selective accretion or diffusion/accretion theory

The composition of the surface layers of λ Boötis stars resembles the composition of the gas phase in the interstellar medium (ISM) [26]. This has led to the theory of selective accretion, where the elements in the gas-phase are accreted onto the stellar surface and dust grains, containing the heavier elements, are blown away by radiation pressure.

The model assumes a star moving through a cloud, excavating a cavity in the cloud by its radiation pressure. The avoidance radius determines the shape and size of the cavity and is dependent on the grain size in the cloud. Fig. 4 is a schematic illustration of the model, while an interesting real example is shown in Fig. 5 (from Gaspar et al, 2008)[1].

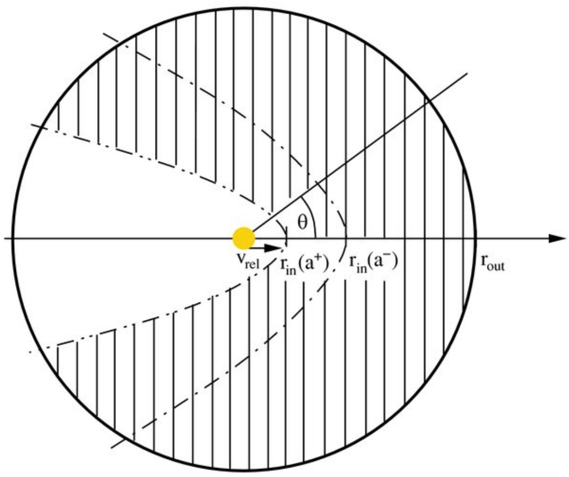

Figure 4: Geometry of the star-cloud interaction. The surface of the cavity is described by the avoidance radius, r_{in}, and the azimuthal coordinate θ. Two different avoidance radii $r_{in}(a^+)$ and $r_{in}(a^-)$ are shown, corresponding to large and small grain sizes, respectively. [14]

A star traveling through an interstellar cloud may have a different effect on different elements in the cloud. Light elements in the interstellar medium are more likely to be in the gas-phase, while heavy elements have condensed into dust grains due to their higher condensation temperature. The dust may then be pushed away by the radiation pressure, while the metal-poor gas may still be accreted onto the stellar surface. The stellar surface abundance is thus lowered in metallicity. This mechanism implies a negative correlation

[1] Note that the example concerns δ Velorum, which is not in the right window of spectral types to be a λ Boötis star. It is however an insightful example for the physical circumstances of the model.

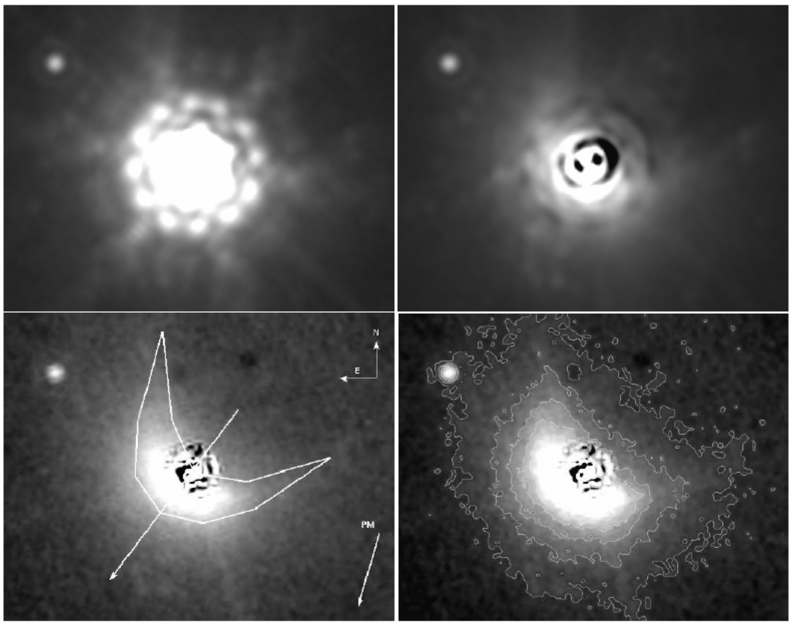

Figure 5: Images of the bow shock around the star δ Velorum, as it plows itself through the surrounding interstellar medium. The images shows the emission at and around the star at 24 μm, with a logarithmic scaling of intensity. Top left panel: the original observed image of star and surrounding medium. Top right: by subtracting the stellar image, the bow shock structure far from the star becomes visible. Bottom left: image of the bow shock structure close to the star. It shows the orientation of the shock and the proper motion direction of the star. The arrow bisecting the bow shock contour shows the calculated direction of the modeled relative velocity. Bottom right panel: same image as the bottom left panel, but with intensity contours superimposed. The intensity contours are at 0.25, 1.0, 1.75, 2.5, and 3.25 MJy sr^{-1} from the faintest to the brightest, respectively. The contours show that the extended emission consists of incomplete spherical shells, centered on δ Velorum. From Gaspar et al. 2008 [6].

between the condensation temperature of elements in the interstellar cloud and the surface abundance of λ Boötis stars. Fig. 6 shows that this correlation is indeed present.

The effect on the surface abundance is only measurable if the star can accrete material efficiently, if it has a shallow convection layer and after the star has traveled a certain amount of time through the cloud. These conditions naturally explain the spectral range and the frequency of the λ Boötis phenomenon. On the lower temperature end stars develop stronger convection zones, quickly diluting any surface anomalies. On the higher temperature end strong stellar winds prevent accretion completely. The chance of a star encountering a cloud is very low and the accretion pattern is washed away in a few million years after exiting the cloud, explaining the small fraction of λ Boötis stars. [12, 14]

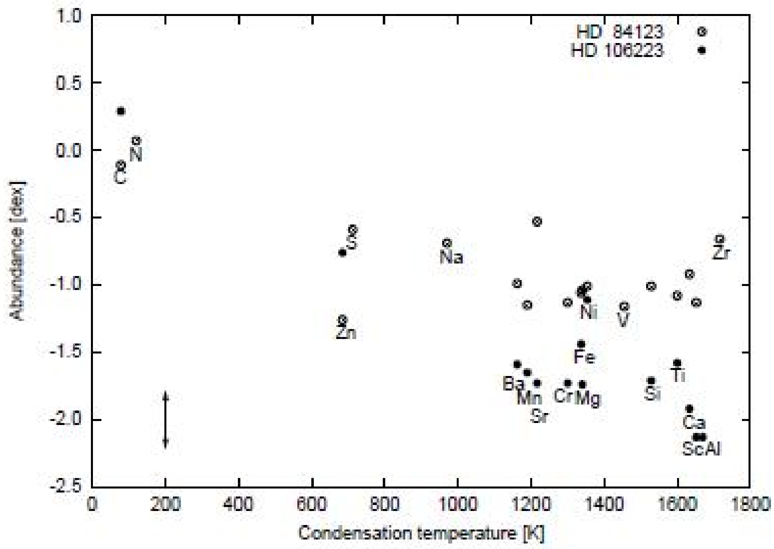

Figure 6: Abundances of the λ Boötis stars HD 84123 and HD 106223 versus condensation temperature. The arrow to the lower left represents the mean error of the abundances [9].

1.3.2 Diffusion with mass-loss

This theory is a modified version of one that has been developed for Am and Ap stars. These show a surplus of heavier elements in their atmosphere, in contrast to the lack of heavier elements in the atmosphere of λ Boötis stars. The theory that explains the higher observed abundance of heavier elements most successfully is based on the build-up of a layered distribution, where each type of element settles in a different layer of the atmosphere. The migration process per element is determined by the balance between its gravitational attraction and radiation pressure. Gravitational attraction pulls elements to lower layers, and radiation pressure levitates them to higher layers, where the radiation pressure per element is dependent on the configuration of its energy levels and the radiation emitted by the stellar surface. Light and un-ionized elements which do not have enough lines to be kept up by radiation pressure such as He, Ne, and O sink to the layers below and heavier elements with many lines such as Mn, Sr, Y and Zr are pushed outward by the radiation field until they have reached an equilibrium position. The heavier elements are therefore observed to be overabundant. [15]

The theory was modified by Michaud & Charland (1986) [16] for λ Boötis stars assuming that they are additionally undergoing a significant mass loss of order $10^{-13} M_{\odot}$ yr^{-1}. The outer layers are then stripped away, revealing the depleted lower layers, leading to the appearance of surface underabundances. However, this model assumes that the stellar atmosphere is stable enough for chemical separation by diffusion processes. This is true for most Am stars, because they are mostly slow rotators without efficient meridional circulation. In the case of Ap stars the atmosphere may be stabilized by a magnetic field.

But the generally fast rotation of λ Boötis stars prevents the stabilization of separated surface layers created by diffusion processes. Moreover, the underabundances materialize only after about 10^9 yr in this scenario, restricting the λ Boötis phenomenon to the end of the main-sequence phase. But λ Boötis stars are often also found relatively close to the zero-age main sequence. So this model does not succeed to explain the λ Boötis pattern [5].

1.3.3 Binaries

An alternative view of the λ Boötis phenomenon relates them to binary stars. Two different binary explanations have been forwarded.

A rather straightforward one is that they involve very close unresolved spectroscopic binary stars. The single but composite spectrum of two quite normal (solar) abundant stars with different effective temperatures and gravities will have a metal-weak character. The imitation would be even more realistic if the components have different rotational velocities. Undetected binarity gives a simple and attractive explanation of the peculiar hydrogen profiles which are typical for most of the λ Boötis stars. However, it remains to be seen whether the strong underabundances found for these stars can be achieved by this model. Moreover, it might be difficult to get a corresponding colour that is in accordance with the spectral range of the λ Boötis stars.

Another scenario was forwarded by Andrievsky [1]. He suggested that λ Boötis type stars can originate by merging as a result of the dynamical evolution of W UMa contact binary systems. These are close eclipsing binary stars with common envelopes whose orbital periods are less than one day. Spectral types of both components are almost always similar, mainly in the range between F0 and K0. Due to angular momentum loss, both components of such a close system approach each other, and finally merge into a more massive but single star. The most essential point is that the merging occurs before both stars finish their main sequence lifetime. Some matter could be lost during the merging phase and form a circumstellar shell. The expectation would be that such stars would have non-standard abundances, including those of CNO. This seems to conflict with the fact that such abundance anomalies of C,N, O and S are not found in most λ Boötis stars [18].

1.4 Research goal

This report describes our study of a set of 33 λ Boötis stars to assess the origin of the infrared excess of this class of stars, in an attempt to decide whether this can be related to the existence of either a circumstellar disk or an interstellar nebula in the stellar environment.

To this end, we have defined a study consisting of the following steps. For each of the stars in our sample, we have determined the wavelength at which the IR excess becomes noticeable. To be able to do this, we first inferred the radius of the stars. These are obtained on the basis of the photometric data at visual wavelengths.

To be able to distinguish between a circumstellar or interstellar origin of the infrared excess we have compared the observed spectral energy distribution (SED) with the theoretic SED. Unique theoretical SED solutions were not possible: the solutions turned out to be degenerate in that the observed SED would allow solutions based on either a circumstellar or interstellar origin.

Therefore, additional information on the nature of the infrared excess has been based on the search for PAH features in the infrared spectrum. If identified, PAH features would be decisive evidence for the interstellar nature and would therefore support the selective accretion model for the λ Boötis phenomenon.

We have also looked whether we could find any characteristic rotational and vibrational molecular lines such as H_2 and CO. This would yield welcome information on the nature of the surrounding medium.

2 Observations and data reduction

In this chapter we present the sample of the 33 λ Boötis stars that have been observed. This involves a description of the sample selection. It is followed by a description of the Spitzer observations of these objects and the SPICE pipeline which we used for the spectral reduction of the observations. The spectra have been combined into a spectral atlas, which is presented in the last section.

2.1 Sample selection

The sample consists of 35 objects in total, selected from the master list composed by Paunzen et al. [19]. The master list contains 57 stars that are confirmed members of the λ Boötes group. Of the stars in the list several astrophysical parameters are specified such as ages, stellar effective temperatures, rotational velocities, surface gravities, distances and luminosities. The 35 stars in our sample are selected according to the following criteria:

- The distance has to be less than 150 pc
- The star has to be brighter than $V = 8$ mag.

This ensures that the observations can be efficiently obtained. Of the original 35 stars only 33 have been observed. The resulting sample is listed in Table 1. The table lists a large number of relevant stellar characteristics for each of the stars [19].

2.2 Spitzer observations

Data has been obtained with the Spitzer InfraRed Spectrograph (IRS) [11] on board the Spitzer Space Telescope [27] between July 2006 and July 2007 (program ID: 30858). The IRS consists of four separate modules (Short-Low, Short-High, Long-Low, Long-High) which provide low (R $\sim$ 60-130) and moderate (R $\sim$ 600) resolution covering the 5.2 to 38 μm range. The observations were carried out using the low spectral resolution modules SL1 (order 1) and SL2 (order 2) in 'mapping mode'. The SL module has a single arsenic-doped silicon (Si:As) array detector which operates over a 5-26 micron wavelength window. The detector properties and wavelength coverage per module order are listed in Table 2.

In mapping mode, spectra may be obtained at different positions around a central target, which allowed us to investigate the interstellar medium. For each target three slit positions were defined: one centered on the star and two on each side of the star with offset positions corresponding to the avoidence radius of the target.

For all spectra the shortest integration time (6 s) has been used. This provides sufficiently high S/N spectra on the source and allows a detection as faint as 11 mJy at of 100 pc of the source with S/N $\sim$ 5-10.

The Spitzer data can be downloaded from the Spitzer Heritage Archive (http://irsa.ipac.caltech.edu/applications/Spitzer/SHA/). For our analysis we downloaded both the Basic Calibrated Data (BCD) and the post-BCD data.

Table 1: Photometric parameters, stellar parameters and calibrated values for the sample of 33 stars (based on Table 1 of Paunzen et al. [19]). The surface gravity log g is photometrically calibrated.

HD	HR	V [mag]	$B-V$ [mag]	$b-y$ [mag]	A_V [mag]	v sin$i$ [km/s]	T_{eff} [K]	log g [dex]	M_V [mag]	log $L_*/L_\odot$
319	12	5.934	0.141	0.079	0.004	60	8020(135)	3.74(8)	1.27(19)	1.45(8)
6870		7.494	0.246	0.164	0.000	165	7330(102)	3.84(11)	2.29(42)	1.02(17)
7908		7.288	0.272	0.192	0.000		7145(87)	4.10(12)	2.60(18)	0.90(7)
11413	541	5.940	0.147	0.105	0.004	125	7925(124)	3.91(21)	1.49(10)	1.35(4)
15165		6.705	0.333	0.191	0.010	90	7010(167)	3.23(10)	1.12(16)	1.50(6)
24472		7.092	0.304	0.214	0.003		6945(131)	3.81(16)	2.14(11)	1.09(5)
31295	1570	4.648	0.085	0.044	0.063	115	8920(177)	4.20(1)	1.66(22)	1.32(9)
35242	1777	6.348	0.122	0.068	0.042	90	8250(103)	3.90(14)	1.75(22)	1.26(9)
74873	3481	5.890	0.115	0.064	0.078	130	8700(245)	4.21(11)	1.82(1)	1.24(1)
75654	3517	6.384	0.242	0.161	0.012	45	7350(104)	3.77(11)	1.83(12)	1.20(5)
84123		6.840	0.297	0.235	0.040	20	7025(175)	3.73(17)	1.58(15)	1.31(6)
87271		7.120	0.172	0.151	0.008		7515(232)	3.43(10)	1.02(8)	1.53(3)
91130	4124	5.902	0.109	0.073	0.000	135	8135(98)	3.78(10)	1.36(26)	1.42(11)
105759		6.550	0.218	0.142	0.000	120	7485(102)	3.65(10)	1.35(21)	1.40(8)
106223		7.431	0.288	0.228	0.015	90	6855(247)	3.49(18)	1.83(45)	1.22(18)
107233		7.353	0.255	0.192	0.048	95	7265(143)	4.03(10)	2.64(13)	0.88(5)
110377	4824	6.228	0.195	0.120	0.000	170	7720(89)	3.97(14)	1.96(11)	1.16(5)
110411	4828	4.881	0.077	0.040	0.045	165	8930(206)	4.14(14)	1.90(28)	1.22(11)
111604	4875	5.886	0.160	0.112	0.000	180	7760(149)	3.61(25)	0.48(7)	1.75(3)
120500		6.600	0.131	0.068	0.017	125	8220(70)	3.86(10)	0.85(34)	1.62(13)
125162	5351	4.186	0.084	0.051	0.039	115	8720(156)	4.07(9)	1.71(23)	1.28(9)
130767		6.905	0.042	0.002	0.000		9195(220)	4.10(8)	1.27(1)	1.48(1)
142703	5930	6.120	0.240	0.182	0.021	100	7265(150)	3.93(12)	2.41(12)	0.97(5)
154153	6338	6.185	0.284	0.199	0.020		7055(120)	3.56(6)	1.86(29)	1.19(11)
156954		7.679	0.294	0.200	0.050	50	7130(93)	4.04(13)	2.81(33)	0.82(13)
168740	6871	6.138	0.201	0.136	0.035	145	7630(81)	3.88(14)	1.82(2)	1.21(1)
170680	6944	5.132	0.008	0.008	0.091	205	9840(248)	4.15(6)	0.83(23)	1.70(9)
192640	7736	4.934	0.154	0.099	0.016	80	7940(96)	3.95(18)	1.84(1)	1.22(1)
193281	7764A	6.557	0.190	0.098	0.111	95	8035(115)	3.54(4)	0.41(30)	1.79(12)
204041	8203	6.456	0.161	0.092	0.026	65	7980(97)	3.97(8)	1.75(18)	1.25(7)
210111	8437	6.377	0.203	0.136	0.000	55	7550(123)	3.84(15)	1.76(15)	1.23(6)
216847		7.060	0.242	0.155	0.000		7355(78)	3.47(14)	0.93(24)	1.56(10)
221756	8947	5.576	0.095	0.056	0.043	105	8510(188)	3.90(3)	1.16(16)	1.50(6)

2.3 Spectral extraction

The Spitzer IRS spectra have been extracted from the BCD with the Spitzer IRS Custom Extraction (SPICE, version 2.0.1), an interactive JAVA-based tool that allows the user to

Table 2: IRS characteristics for all three orders of the Short-Low module. SL3 is a 'bonusorder' that covers the 7.3-8.7 micron spectral region in first order when the source falls on the second order, which may be used for normalizing the first- and second-order segments of the spectrum.
* The resolving power $R = \lambda/\mathrm{d}\lambda$ is approximately constant as a function of wavelength within each order.

Module/ order	Channel	Detector	Wavelength range (μm)	Resolving power*	Plate scale (″/pix)	Slit width (″)	Slit length (″)
SL2			5.13-7.60	60-127		3.6	
SL3	0	Si:As	7.33-8.66		1.8		57
SL1			7.46-14.29	61-120		3.7	

perform non-default extractions. IRS spectra are not rectilinear on the array, so spectral extraction requires careful tracing of the shape of each order. SPICE visualizes the extraction window and provides the tools to properly perform the extraction. The software can be run for a single BCD frame, or in batch mode for processing of many exposures. The SPICE pipeline essentially follows the same procedures as the general Spitzer pipeline, so consistent results may be obtained.

The pipeline involves the following modules:

- **Profile**

  The BCD for the SL module is a long-slit 2-D spectrum spanning position and wavelength. First we need to determine the exact position from where to obtain the spectrum. The Profile module averages the flux per position over all wavelengths of all orders in the slit, creating an average spatial flux profile. The source is at the position with the highest flux, which will be determined in the Ridge module.

  The input files for the Profile module are the BCD image in FITS format *bcd.fits* and the calibration file *wavsamp.tbl*. The latter specifies the location of the selected spectral orders. By default all available orders are used in measuring the spatial profile. The user may also choose the orders from a pulldown menu.

  The output file for the Profile module is *profile.tbl*, a table of the wavelength-collapsed average spatial profile for the selected orders. The graph of flux vs. position (percentage along the spatial direction of the slit) is shown in the plot window.

- **Ridge**

  The Ridge module identifies the location for point source extraction by determining the peak in the spatial flux profile created by the Profile module. The user may also specify a fractional location along the slit, enabling the user to extract spatial information at any position along the slit.

The module takes as input the file *profile.tbl* and the two calibration files *wavsamp.tbl* and *psf_fov.tbl*. The latter contains information on the point spread function (PSF) and field of view (FOV). If no candidate peak is found the peak is set to the expected position of the field of view as defined in the *psf_fov.tbl* file.

Once the peak is determined, the Ridge module computes the ridge line in the BCD frame. It outputs the table *ridge.tbl*, containing the ridge line in the form of the IRS array coordinates (x,y) of the peak for each order and each wavelength. The ridge line is visualized with an overlay on the input image.

- **Extract**

  The Extract module extracts the one-dimensional spectrum for either point or extended sources.

  It takes as input the file *bcd.fits* and extracts the 1-D spectrum along the trace defined in *ridge.tbl*. It also takes as input the associated uncertainty in *func.fits* and the files *psf_fov.tbl* and *bmask.fits*. The mask file identifies fatally masked pixels that will be excluded from the extraction.

  The output of the module is the 1-D extracted spectrum, in units of electron/sec, written to the table *extract.tbl*. It includes the order, wavelength, flux, propagated error and pixel status of the contributing pixels for each wavelength.

- **Point source tune**

  The Point source tune module applies absolute flux calibration to the 1-D spectral output file from the Extract module. The fluxes are converted to Jansky, and the module corrects the slope and curvature of each order by applying the polynomial coefficients in the *fluxcon.tbl* file. This correction is based on an order-by-order comparison of calibration data to standard star model spectra.

  The module takes the output file from the Extract module *extract.tbl* and the calibration file *fluxcon.tbl* as input.

  The output is the flux calibrated spectrum *spect.tbl*. It contains 5 columns listing the order number, wavelength in micron, flux and uncertainty in flux in Jy and pixel status per wavelength. It is written to the output table and displayed in the plot window.

- **Extended source tune**

  The Extended source tune module applies the same steps as the Point source tune module, but optimized for extended sources. It assumes an extended source which is uniformly bright and covers an area much larger than the slit. In practice, the calibration will be approximately correct for sources that are uniform over the width of the slit plus several PSF widths ($\sim$ 6 pixels) on either side.

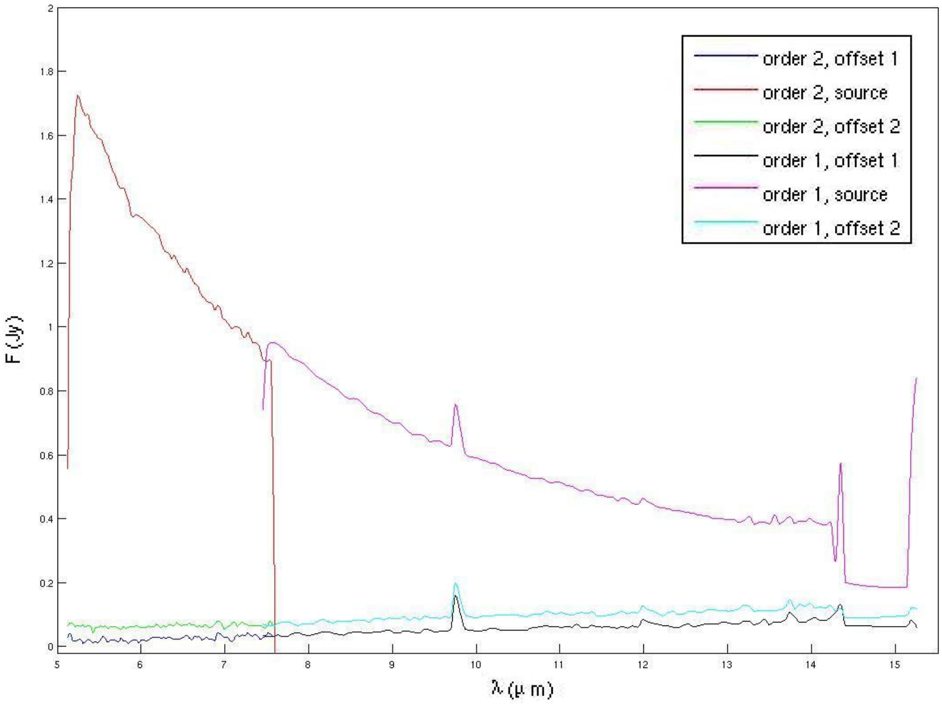

Figure 7: A first look at the raw obtained spectra for HD110411. The higher line is the spectrum of the source, the lower lines are the spectra of the offset positions. Edge effects are not yet cut off.

2.4 Spectral atlas

All 33 stars of the sample have been extracted following the procedure outlined above. In all cases, default parameters for the different procedures have been adopted. A visual comparison with the post-BCD demonstrated that this leads to reliable results. An example of the spectrum as obtained by SPICE is seen in Fig. 7. The flux at the source is considerably higher than that at offset positions. Also, we see that in this wavelength regime the stellar spectrum decreases systematically with wavelength as expected for a blackbody of a temperature of 9000 K. On the other hand, the flux at the offset positions increases weakly, but consistently over the same wavelength regime. This corresponds to the thermal emission of dust with a temperature of roughly $T_{eff} \sim$ 100-200 K. In a follow-up study we intend to systematically investigate the properties of the dust in the stellar environment of our sample.

In order to examine the spectral features more closely, the continuum has been subtracted with a first-order determination of the slope of the spectrum. Effectively this means that the blackbody continuum of star and dust have been removed. A comparison

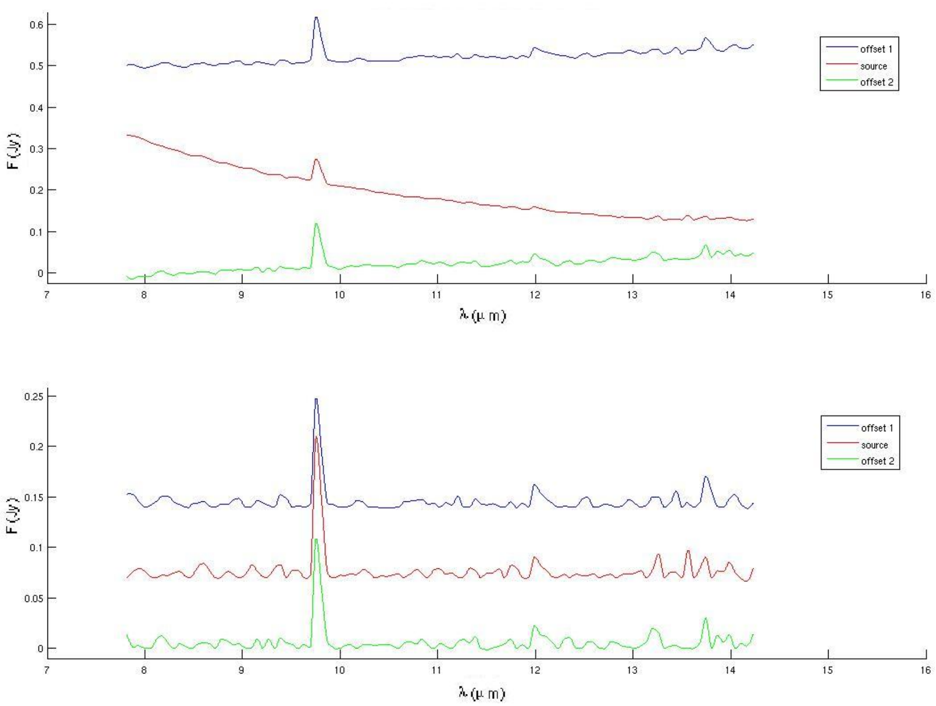

Figure 8: A comparison of the original flux (top panel) vs. the continuum-subtracted flux (bottom panel) for HD110411.

between the original flux and the continuum-subtracted flux for HD110411 is made in Fig. 8. The top frame shows the order 1 spectra for all three slit positions, one centered on HD110411 itself and two at the offset positions. Note that the fluxes at the different positions are relative fluxes, and for cosmetic reasons the stellar spectrum has been placed in between the two offset spectra. The corresponding continuum-subtracted spectra are shown in the bottom frame. We clearly recognize identical spectral features in the three spectra. However, the most prominent line at 9.7 μm turned out to be due to instrumental damage (also see the discussion in Sect. 3.4).

The final product of this analysis is an extensive atlas of NIR continuum-subtracted spectra for the 33 stars of our sample. Of each of these objects, the atlas involves all 3 slit positions (the source and two offset positions). The atlas contains the spectra of all objects in our sample, combined in one plot per 11 stars to facilitate the comparison between them. An example of such an atlas plot is shown in Fig. 9, in this case the order 1 spectra of the second offset for the eleven stars specified in the legend.

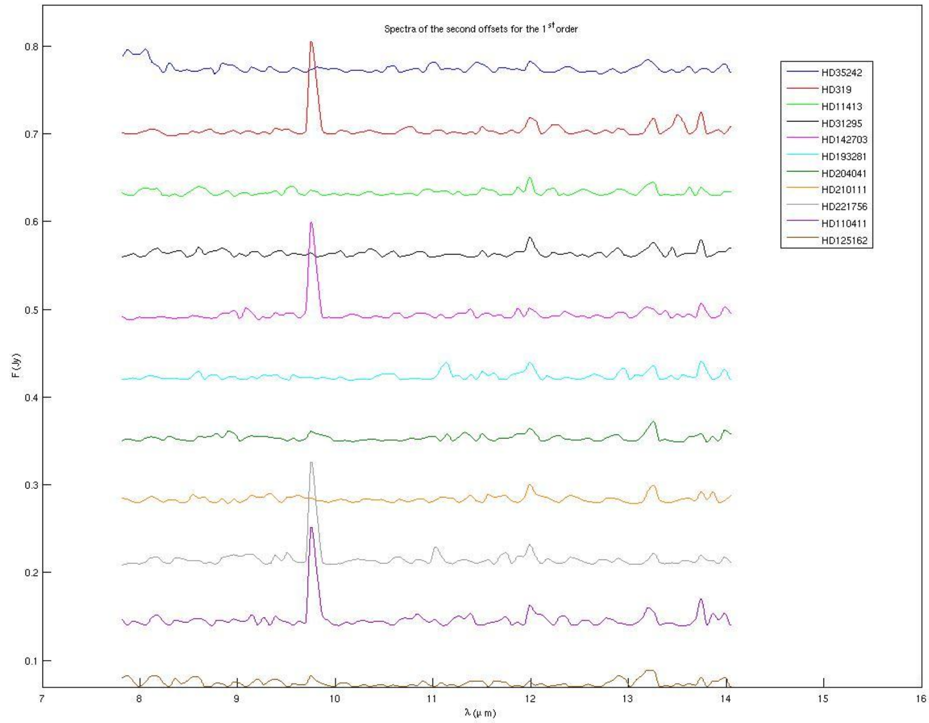

Figure 9: An example of a comparison of the order 1 spectra of the second offset of 11 stars in the sample.

2.5 Instrumental problems

The Spitzer pipeline takes care of most instrumental problems that might occur, but some data caveats remain. These have affected various cases of our sample (see Sect. 3.4).

- Semi-permanent bad pixel conditions are not always included in the Spitzer rogue pixel mask and may not always be cleaned by IRSCLEAN. Apparent line features need to be checked for bad pixel conditions before a conclusion can be drawn.
- The Short-Low module on the IRS suffers from excess emission between 13.2 and 15 μm. This excess emission is referred to as the '14 μm teardrop feature' and may be caused by scattered light (see Fig. 13). Even though recent Spitzer calibrations have isolated this feature from fits to the calibrator spectra, it is still present in the data. This might be misinterpreted for an emission of small grains.

3 Data analysis

We first describe a method to determine the onset of the IR excess from the Spitzer spectra, by comparing them to ATLAS9 stellar atmosphere models with the appropriate stellar parameters. The calculation has been performed for HD 110411 and may be applied to all stars. The onset of the IR excess will give an indication for the size of the debris grains in the stellar environment and may thus help to distinguish between larger circumstellar dust and smaller interstellar dust. The radii of the stars are first derived by comparison of observed photometric magnitudes with synthetic magnitudes obtained from the ATLAS9 models in the visual spectral regime.

Subsequently, we have looked for the presence of polycyclic aromatic hydrocarbons (PAHs) in the spectra since these would be a convincing evidence for interstellar material rather than circumstellar. Finally, we have studied the possible presence of rotational-vibrational lines in the spectra. One of our findings is that instrumental artefacts have played a substantial role in the data.

3.1 ATLAS9 models

We have compared the photometry of our sample of stars with the ATLAS9 models of stellar atmospheres. The ATLAS9 grid of model atmospheres is computed by Castelli & Kurucz with the ATLAS9 program of Kurucz. The original atlas (CD-ROM No. 13) can be obtained from Dr. R. Kurucz. A recent description of the models can be found in Castelli & Kurucz (2004) [4].

The ATLAS9 atlas contains about 7600 stellar atmosphere models for a wide range of metallicities, effective temperatures (T_{eff}) and gravities ($\log g$). The atlas includes models of abundances [M/H] = $\log(Z/Z_{\odot}$ = +1.0, +0.5, +0.3, +0.2, +0.1, +0.0, -0.1, -0.2, -0.3, -0.5, -1.0, -1.5, -2.0, -2.5, -3.0, -3.5, -4.0, -4.5, and -5.0. The grid of models cover the gravity range from log g= 0.0 to +5.0 in steps of +0.5. The range in effective temperature from 3500 K to 50000 K is covered with an uneven grid. Kurucz and Castelli also computed model grids for several microturbulent velocities. The model spectra cover the ultraviolet (1000A) to infrared (10 microns) spectral range with non-uniform wavelength spacing.

The ATLAS code was originally presented and extensively described in 1970 by Robert Kurucz [13], using the assumption of local thermodynamic equilibrium (LTE) and hydrostatic and plane parallel atmospheres. Later on, Castelli extended Kurucz's models by computing some more grids for metallicities with enhanced α elements abundances (such as O, Ne, Mg, Si, S, Ar, Ca, Ti) by 0.4 dex over the solar abundance. Since the source code is publicly available on the web, it has been amended by different persons numerous times over the years and nowadays exists in many versions. There are both plane parallel and spherical versions as well as those using opacity sampling or opacity distribution functions.

For the subject of this thesis, it is also interesting that Castelli & Kurucz carried out a detailed computation of the UV spectrum of λBoo [3].

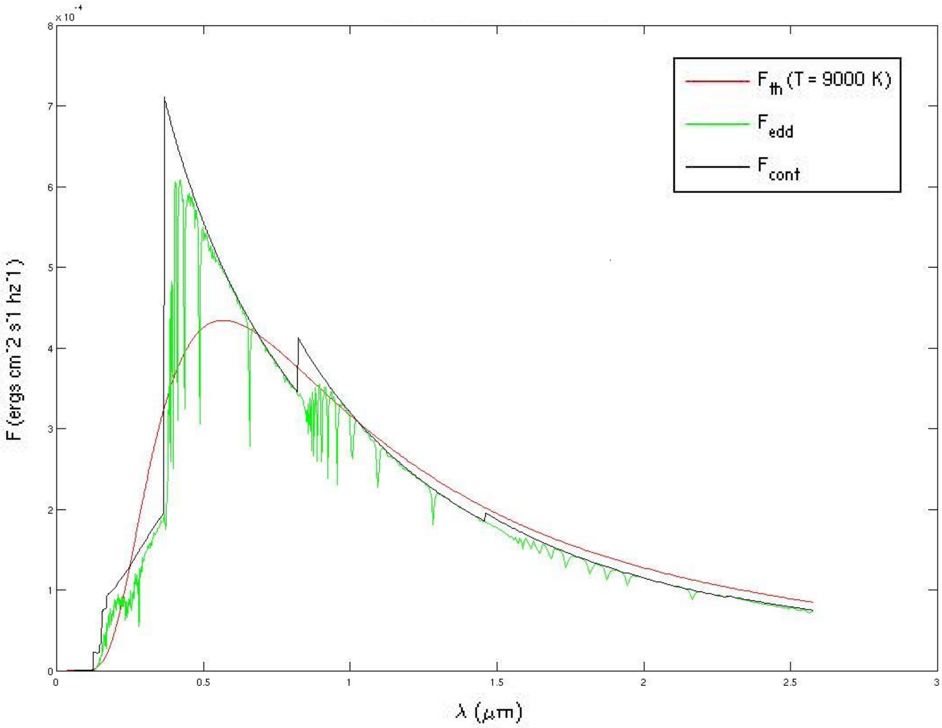

Figure 10: The Eddington flux F_{edd} and continuum flux F_{cont} for an ATLAS9 model for a star with surface temperature $T = 9000$ K, surface gravity log $g = 4.5$ and solar metallicity as a function of wavelength. A theoretical curve for a blackbody with a temperature $T = 9000$ K is plotted over the ATLAS9 spectra for comparison.

3.2 Photometric data and infrared excess

Previous infrared measurements of our sample of λ Boötis stars have already indicated the presence of dust in their environment. We verify the infrared excess independently for the new IRS Spitzer spectra and establish the onset of the excess to examine its physical nature. The observed infrared flux is compared for this purpose with the predicted flux from the Kurucz ATLAS9 models for a given surface temperature T_{eff}, surface gravity g and metallicity m. The emitted stellar energy predicted by the ATLAS9 models by a star with radius R is assumed to be radiated isotropically, so that the predicted observed flux $F_{\nu,\oplus}$ on Earth (at a distance D from the star) is

$$F_{\nu,\oplus} = F_\nu \left(\frac{R}{D}\right)^2 , \tag{1}$$

where F_ν is the emitted flux at the stellar surface per frequency ν, given by the ATLAS9 models. The parallax angle p for all stars in our sample has been measured by the

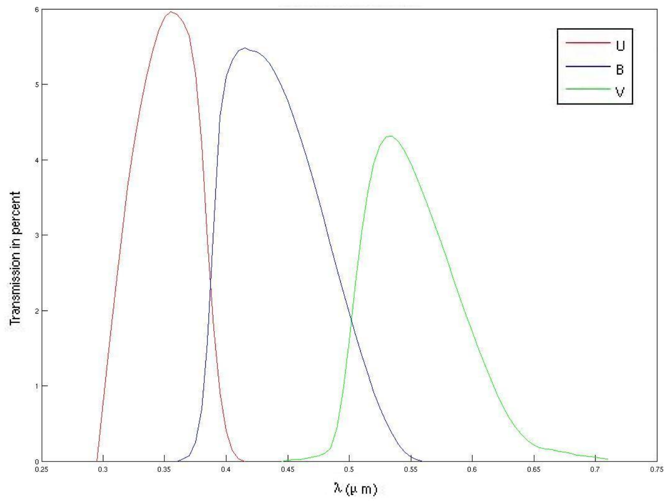

Figure 11: The transmission of the filters in the UBV-Johnson system in percentage.

Hipparcos satellite [20], so the distances can be computed with

$$D(\mathrm{pc}) = \frac{1}{p(\mathrm{arcsec})} \ . \tag{2}$$

The only unknown remains the stellar radius R. To determine this, we proceed as follows. We assume that the stellar spectra in wavelength bands from the infrared to the ultraviolet are well-predicted by the ATLAS9 models, and we compare these with existing photometric measurements. The stellar radius is then

$$R = \sqrt{\frac{F_{\nu,\oplus}}{F_\nu}} D \ , \tag{3}$$

where $F_{\nu,\oplus}$ is the measured flux on Earth in a certain photometric band and F_ν is the predicted flux at the stellar surface in that band for the ATLAS9 model. The latter is determined by applying the method of *synthetic photometry* to the ATLAS9 data. This is a numerical algorithm that computes theoretical magnitudes and colors in a photometric system from a spectral energy distribution (SED) and the response functions of the photometric system.

The basic equation of synthetic photometry convolves the observed or model atmosphere flux f_λ as a function of the wavelength λ with the response function S_i of the i-th filter in a photometric system with n filters to retrieve the mean flux density in that passband:

$$F_\lambda(S_i) = \frac{\int_o^\infty F_\lambda(\lambda) S_i(\lambda) \mathrm{d}\lambda}{\int_0^\infty S_i(\lambda) \mathrm{d}\lambda} \ . \tag{4}$$

In this equation the mean flux density weights each detected photon in proportion to its energy. The response function is a product of the characteristic functions of all individual components that contribute to the total observed flux, including the filter transmission, the mirror reflectivity and the quantum efficiency of the detector.

Eq. (4) is evaluated by numerical integration of the flux distribution over the passband function $S_i(\lambda)$. We have used the passbands of the UBV-Johnson photometric system, see Fig. 11. Where necessary, we convert the flux per wavelength unit interval to the flux per unit frequency interval. The relation between F_λ and F_ν is given by

$$\begin{aligned} F_\lambda &= F_\nu \left| \frac{\mathrm{d}\nu}{\mathrm{d}\lambda} \right| \\ &= F_\nu \left| \frac{\mathrm{d}\,(c/\lambda)}{\mathrm{d}\lambda} \right| \\ &= F_\nu \frac{c}{\lambda^2} \end{aligned} \tag{5}$$

For astronomical purposes, we often use magnitude instead of flux. The synthetic magnitude m_i for passband S_i is calculated according to

$$m_i = -2.5 \log F_\lambda(S_i) + k_i \ , \tag{6}$$

where k_i defines the zero-point for passband i. The synthetic color c_{ij} is the magnitude difference between passband i and j and is defined as

$$c_{ij} = m_i - m_j \ . \tag{7}$$

The above calculation has been performed for HD 110411. The resulting stellar radius was found to be $1.5 \pm 0.1\ R_\odot$. This corresponds to the radius of $1.6\ R_\odot$ found by Martínez-Galarza [14].

The Spitzer spectra may now be compared to the ATLAS9 spectra to assess the onset of the IR excess. The ATLAS9 spectra have sufficient wavelength resolution for our investigation up to 10 μm. Instead of using the rather sparsely resolved ATLAS9 spectrum from that wavelength onward, we chose to use a blackbody continuation. The effective temperature T_{eff} is determined from the ATLAS9 flux at 10 μm. The resulting specific intensity or brightness I_ν that is radiated on wavelengths in excess of 10 μm is given by the Planck law:

$$I_\nu = \frac{2h\nu^3/c^2}{e^{h\nu/kT_{eff}} - 1} \tag{8}$$

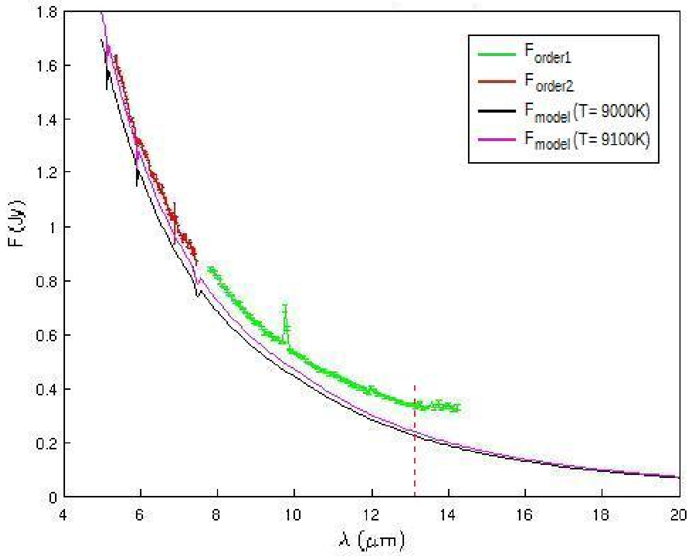

Figure 12: The Spitzer spectrum for HD 110411 compared to ATLAS9 models for T = 9000 K and T = 9100 K. The ATLAS9 models are continued with a blackbody spectrum from $\lambda = 10.0$ μm. At first sight it appears as if the flux slope increases significantly with respect to the ATLAS9 models from $\lambda = 13.2$ μm (red dotted line). But this is an artefact due to the teardrop feature. However, the slope still increases slightly before that point with respect to the ATLAS9 models, which does indicate the onset of the IR excess.

A possible complication arises as a result of the peculiar metallicity of the λ Boötis stars. The lower metallicity of the stars results in a higher UV flux, as less of the UV radiation gets absorbed by metal line blanketing in the stellar atmosphere. If the UV flux is dimmed by line blanketing the absorbed energy must be re-rediated which is usually in the red or infrared part of the spectrum. Thus, the higher UV flux in metal-poor stars goes along with a corresponding lower flux in the infrared regime. Since we have used solar abundances for the ATLAS9 models, the estimate of the infrared excess may be underestimated. However, the effect is large in the UV, but small in the infrared. The new stellar atmosphere models for λ Boötis stars by Kurucz [3] might provide a better estimate.

3.2.1 Infrared excess

In Fig. 12 we compare the Spitzer spectrum for HD 110411 with that of ATLAS9 models for T = 9000 K and T = 9100 K. The ATLAS9 models are continued with a blackbody spectrum from λ=10 μm onward. We observe a considerable and increasing difference, a manifestation of the deviating slopes of the two spectra. We identify two aspects of this difference. There is a sudden increase of slope from $\lambda = 13.2$ μm onward. However, this is due to an artefact which we indicate by the name of *teardrop* feature (see Sect. 2.5 and

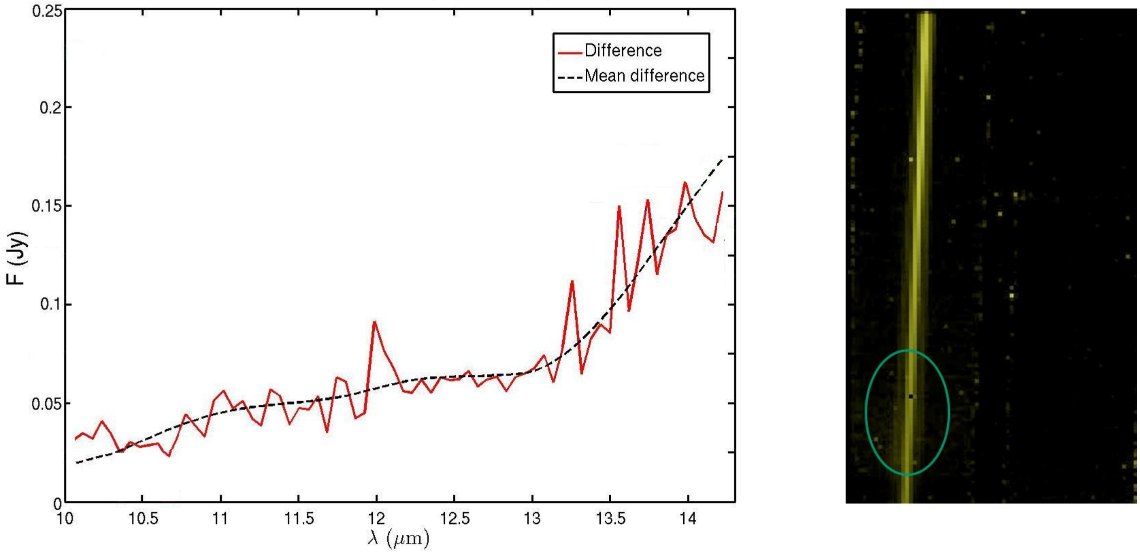

Figure 13: Left: the difference and mean difference between the Spitzer data for HD110411 are compared to the ATLAS9 model for $T = 9000$ K. Up to 13.2 μm a slight difference with the model is seen, but the excess beyond that point is caused by the teardrop feature. The figure on the right shows the illuminated spot between 13.2 and 15 μm in the basic calibrated data which causes the teardrop feature.

Fig. 13).

A real difference with the ATLAS9 models is found already at a slightly shorter wavelength. This is the onset of a real infrared excess, whose identification is one of the targets of the research project. One explanation is that this IR excess is due to the presence of dust in the vicinity of the star. The wavelength at which this excess becomes noticeable is an indication for the size of the dust particles, and for our study represents the main result. When this occurs at 10 μm, as it appears for HD 110411, they are rather small and thus more likely interstellar in nature.

To confirm whether the infrared excess is real, we compared the ATLAS9 spectrum with the mid-infrared IRAS fluxes observed for HD 110411. In the log-log plot of Fig. 14 we see that the three IRAS datapoints reveal a large excess with respect to the model spectrum.

3.2.2 Circumstellar nebula or debris disk

Finally, we have used the photometric data for a comparison with the models described in Martínez-Galarza [14]. Fig. 15 shows four model spectra. The model spectra were kindly provided by Juan Rafael Martínez-Galarza. Three of these concern a dust disk surrounding the star. One disk has a temperature of 60 K, the second a temperature of 80 K and a third one a temperature of 100 K. In addition, we have a model based on the

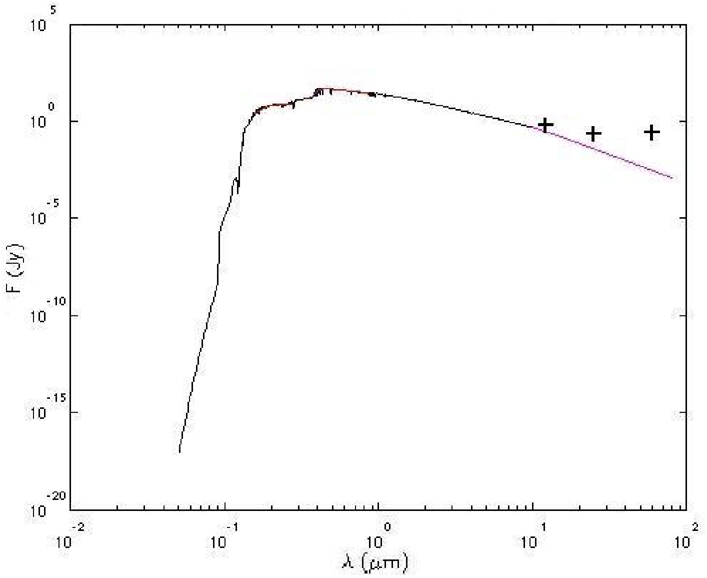

Figure 14: The ATLAS9 model spectrum for a star with the temperature of HD 110411, including the blackbody continuation for wavelengths larger than 10 μm. The three datapoints (plus signs) are IRAS fluxes for 12, 25 and 60 μm. Unlike the previous figure, the spectrum has been plotted log-log.

presence of diffuse interstellar cloud.

The ATLAS9 model for T=9000 K, continued with a blackbody beyond λ = 10μm, agrees very well with all models up to 13μm. Beyond that wavelength it starts to differ strongly from the other models. In order to constrain the models we need data at longer wavelengths. To this end, we include three IRAS data points, at 12, 25 and 60 μm. These clearly indicate an excess with respect to the ATLAS9 model. However, they are not able to distinguish between the different disk models and the diffuse cloud model. The datapoints seem to agree reasonably well with all four models within 3σ.

This conclusion shows that SED modeling alone is not suffficient to distinguish between an interstellar reflection nebula and a debris disk. For this reason, we are going to study the Spitzer spectra of the stars to search for the presence of spectral features that are unique to the ISM.

3.3 PAH features

A strong argument for the presence of an interstellar nebula would be the detection of polycyclic aromatic hydrocarbons (PAHs). PAHs are organic compounds which are composed of two or more linked aromatic rings (e.g. benzene rings). The simplest PAH is naphthalene, a fused pair of two benzene rings. PAH molecules exhibit characteristic broad emission features in the near and mid-IR, predominantly at wavelengths of 3.3, 6.2, 7.7, 8.6 and 11.3 μm. These features are observed in various astrophysical environments,

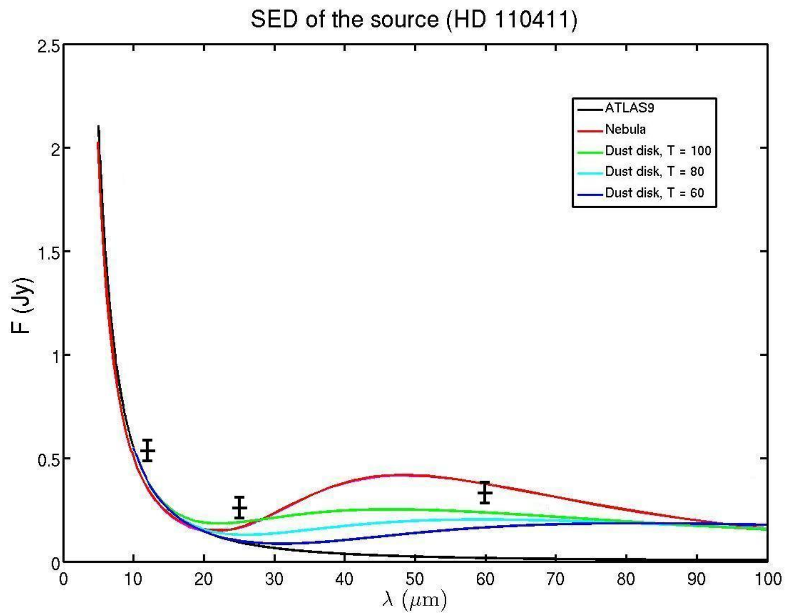

Figure 15: The ATLAS9 model for $T = 9000$ K (which is continued with a blackbody beyond 10 μm) compared with the model in which a star travels through a diffuse interstellar cloud, and 3 models with a dust disk of different temperatures (60, 80 and 100 K) surrounding the star. The ATLAS9 model agrees very good with all models up to 13 μm. Three IRAS data points at 12, 25 and 60 μm with 1σ errorbars are included for comparisons at longer wavelength.

such as the diffuse interstellar medium, planetary nebulae, photon dominated regions, and protoplanetary disks, indicating that they are an important and common component of the interstellar medium [25]. So far, PAH features have not been detected in older debris disks. Therefore the detection of the characteristic emission of PAHs would be direct evidence for the presence of an interstellar nebula around λ Boötis stars.

We have investigated the presence of PAH features in the spectra of the offset positions using PAHFIT (version 1.2). PAHFIT is an IDL tool for decomposing low-resolution Spitzer IRS spectra of PAH emission sources. It uses a model consisting of a stellar and thermal dust continuum in fixed temperature bins, resolved dust features and feature blends, prominent emission lines and dust extinction, dominated by the silicate absorption bands at 9.7 and 18 microns. [24]

We have run PAHFIT on the spectra of several stars of our sample. The results for HD193281 are shown in Fig. 16(a). HD193281 is chosen here because its spectrum does not contain the 9.7 μm peak, which was later shown to be caused by a hot pixel (also see the discussion in Sect. 3.4). The reduced $\chi^2 = 14.038$. This indicates that the expected PAH features, i.e. the 3.3, 6.2, 7.7, 8.6 and 11.3 μm lines, do not provide a good fit to the data.

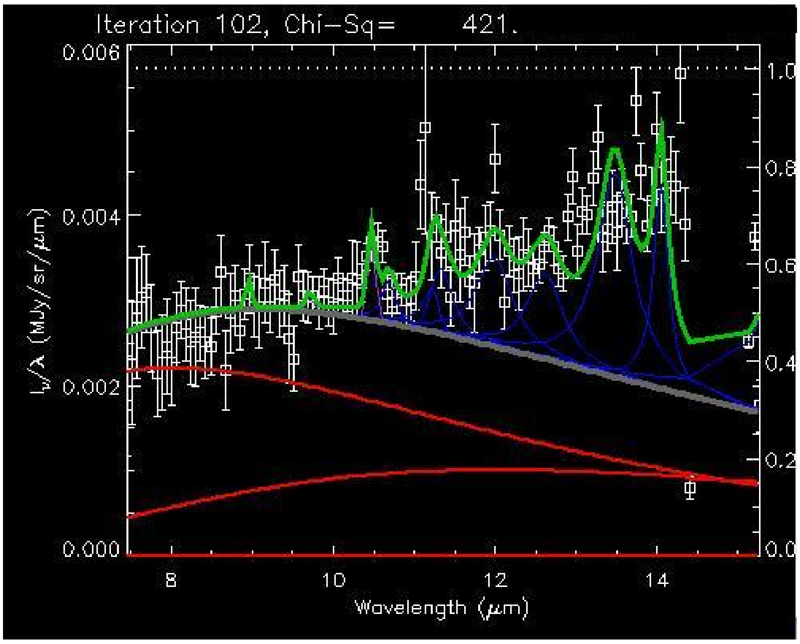

(a)

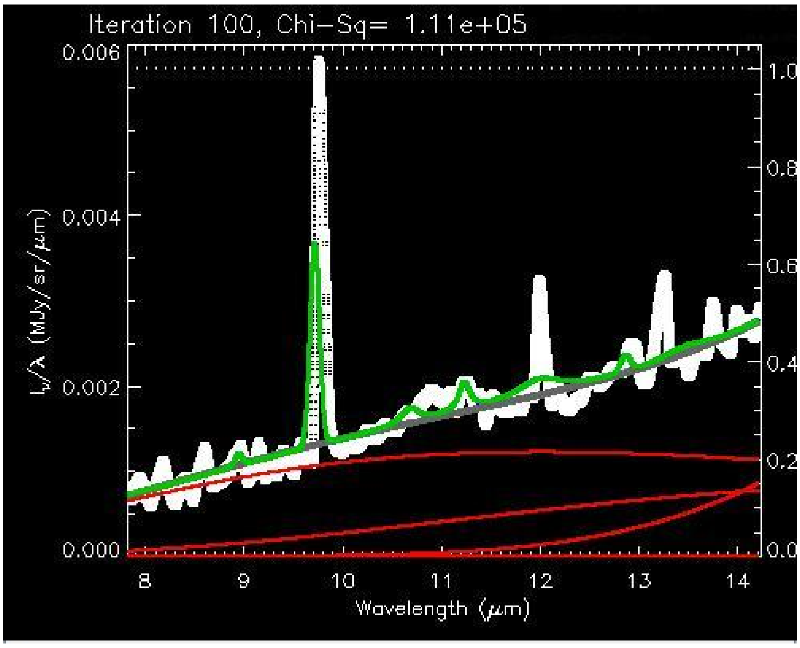

(b)

Figure 16: PAHFIT decompositions for the spectrum of HD193281 from 7.4 - 14.5 μm (panel (a)) and of the average sample spectrum (panel (b)). Red solid lines represent thermal dust continuum components. The thick gray line represents the total (dust + stellar) continuum. Blue lines above the total continuum are dust/ PAH features. The solid green line is the full fitted model.

To assess whether any of the PAH features could be traced in any of the other spectra in the sample we have averaged the sample spectra. Subsequently, we ran PAHFIT on this average sample spectrum. If PAH features are present in any of the spectra, this average spectrum should at least show weak PAH features. The results for the average spectrum are shown in Fig. 16(b). The reduced χ^2 is 17.620. It confirms the lack of PAH features in any of the sample spectra.

3.4 Molecular spectral features

In addition to the PAH features there may have been spectral signatures of other molecular species in the IR spectra of stars in our sample. Despite the low resolution of our spectra (see Table 2) strong lines may still be observed. One may think of various molecular species, starting with the simplest bi-atomic molecule, molecular hydrogen, H_2. Molecular spectral lines may relate to three different transitions (see [21], chapter 11). One class is that of electronic transitions, involving the jump of an electron to another energy level in the molecule. More characteristic for molecules are vibrational and rotational transitions. Rotational transitions are related to changes in rotation rate of the atoms in the molecule with respect to each other. Likewise, vibrational transitions involve a change of vibration energy of the atoms with respect to each other.

In the ground state, the easiest way to excite a molecule into higher energy states is to cause the molecule to rotate. The energy needed to excite a vibrational mode or an electronic state is much greater than typical rotation energies. Therefore, it is possible to have transitions solely among the rotational states when the molecule is in its lowest vibrational and electronic states [21].

For example, for a diatomic molecule like H_2 or CO, we may consider the rotational energy levels J of the molecule,

$$E_J = \frac{\hbar^2}{2I} J(J+1) \ . \tag{9}$$

In this expression, I is the moment of inertia about the axis between the two atoms and J is the angular momentum quantum number. Strict selection rules determine whether a molecule can jump from one angular momentum state J to another J', accompanied by the emission or absorption of radiation. In case it would involve a molecule with a nonzero dipole moment, the selection rules would be [21]

1. ΔJ=-1 (emission)

2. ΔJ=1 (absorption)

In the above, $\Delta J = J' - J$. Note that such radiative transitions between rotational levels are only possible if the molecule has a dipole moment. The most common molecule in the Universe, H_2, does not have an electric dipole, just like other molecules with identical atomic nuclei [10]. Therefore, no electric-dipole allowed transitions exist for H_2. At lower transition probability electric *quadrupole* transitions are allowed with $\Delta J = \pm 2$.

We should also take account of the transitions between different vibrational levels. Because the energies required to excite vibrational modes are much larger than those required to excite rotation, usually these involve transitions between both vibrational and rotational levels. The vibrational energy level of a molecule is characterized by its vibrational quantum number v. In the case we would approximate the vibration by an harmonic oscillator, the vibrational energy of a level v would be given by

$$E_{nv} = \hbar\omega_{nJ}(v + \frac{1}{2}) \tag{10}$$

where ω_{nJ} is the rest frequency for electronic state n and rotational level J. The corresponding vibrational-rotation transition involve a more elaborate set of selection rules, involving dipole conditions, and allowed jumps in vibration quantum number v and rotational quantum number J. In fact, the molecular spectral lines may be classified according to the rotational "fine-structure", following the change in J. It leads to the identification of so-called molecular "branches" [21, 10]:

$$\begin{aligned}
\Delta J &= -2: && \text{O branch} \\
\Delta J &= -1: && \text{P branch} \\
\Delta J &= 0: && \text{Q branch (when allowed)} \\
\Delta J &= 1: && \text{R branch} \\
\Delta J &= 2: && \text{S branch}
\end{aligned}$$

In each of these branches, we identify lines by a pair of numbers accompanying the branch letter. The pair identifies the corresponding vibrational transition. For example, 0-0 S(0) indicates that the transition occurs in the vibrational ground level. On the other hand, 1-0 S(0) corresponds to a change from vibrational level 1 to level 0. The number in between brackets indicates the final rotational level J, and determines the rank of the line in the given branch.

The Spitzer spectra of our sample cover the 5-14 micron wavelength regime which may be used to study the fundamental vibrations and associated rotational-vibrational structure. We have searched the sample for characteristic spectral features of this class. The most prominent spectral feature is the line at 9.7 micron, see for example Fig. 8. The most likely candidate for this line was the H_2 0-0 S(3) line at 9.66 micron. This line might be expected in a shock region, which may be present if the star travels through an interstellar nebula (see Fig. 5). We have compared this line with the line in the different stellar spectra and with an average spectrum taken over all stars, see Fig. 17. We concluded:

- The line does not fit exactly at the right position. The line might however be Doppler shifted. In the case that the line originates in a bowshock, a maximum velocity of 300 km/s is adopted to calculate the maximum Doppler shift. The line intervals in Fig. 17 indicate the possible wavelengths for the H_2 0-0 S(2), S(3) and S(4) lines with a maximum Doppler shift corresponding to 300 km/s. We have concluded that the 9.7 micron peak cannot be identified with the S(3) line.

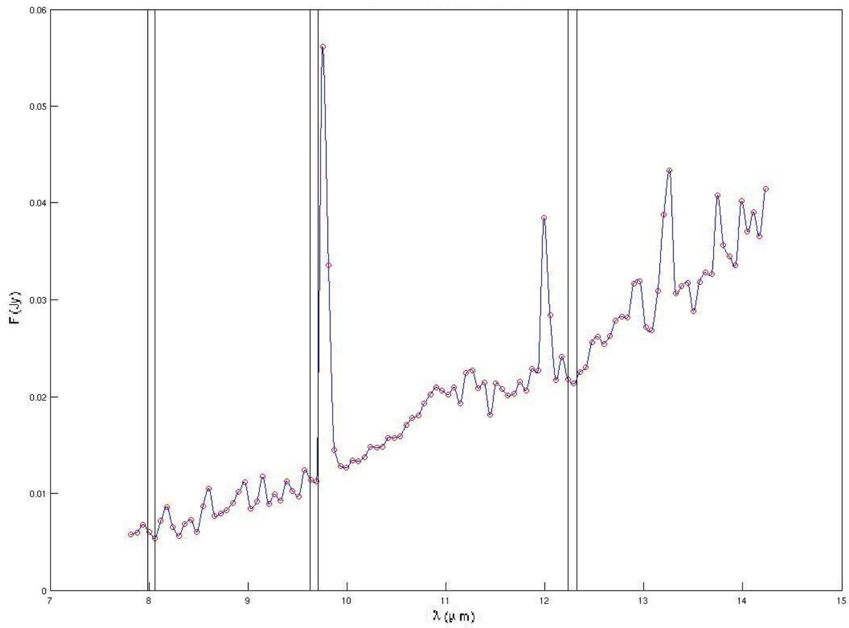

Figure 17: The averaged spectra of all stars in the sample compared to the H_2 0-0 S(2), S(3) and S(4) lines at 8.03 μm, 9.66 μm and 12.28 μm, respectively. The solid vertical lines indicate the minimum and maximum observed wavelength of each line considering a maximum Doppler shift expected from a shocked gas with v_{shock} = 300 km/s. The 9.7 μm peak clearly does not fit in the spectral window for the H_2 0-0 S(3) line.

- If the S(3) line would have been present, the S(2) and S(4) lines which lie between 5-14 micron would be expected to be present as well. These lines are however not detected.

We conclude that we have not found any rotational H_2 lines. We have also looked for CO_2 lines and several other candidates in spectral line lists, but none of these could be fit to the observed peaks in the spectrum.

3.5 Instrumental artefacts

We have investigated the peak at 9.7 μm further to determine its cause and have come to the conclusion that it is due to a temporarily hot pixel. There are two reasons why the feature is not always present:

1) Pixels are not always hot; bad pixels can also be temporarily hot, see Fig. 18 and 19. The Spitzer website defines ill-behaved or 'rogue' pixels as pixels that are permanently or temporarily hot. And thus also something in between can occur, which explains the

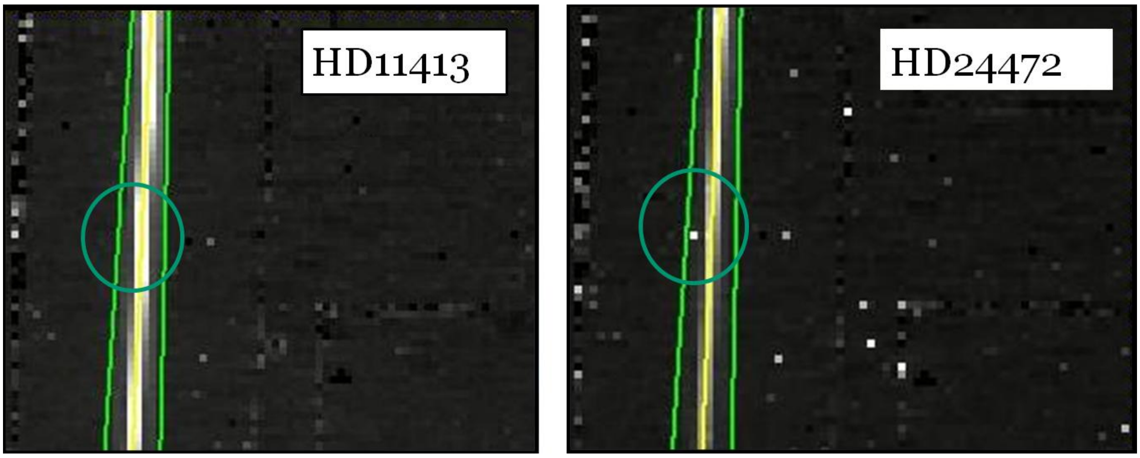

Figure 18: The basic calibrated data files for HD 11413 and HD 24472. The green lines indicate the calibrated slit definition by SPICE. The hot pixel in the circle on the right is responsible for the 9.7 μm peak (compare with Fig. 19(d).)

different amplitudes of the 9.7 μm feature. We have not found a technical explanation on the instrumental level yet.

2) SPICE does not always use the same slit definition. The slit may be very differently chosen by SPICE for the different objects, so that the hot pixel is not always included.

In hindsight, inspection of Fig. 7 would also reveal that the 9.7 μm feature is equally strong in both the stellar spectrum and the offset spectra. This is unlikely and therefore more likely to be an instrumental artefact.

Fig. 19 reveals that more pixels may be subject to instrumental damage. The data will need to be cleaned from these instrumental artefacts in order to obtain reliable spectra. We intend to use the Spitzer IRSCLEAN software to clean the data in a follow-up research.

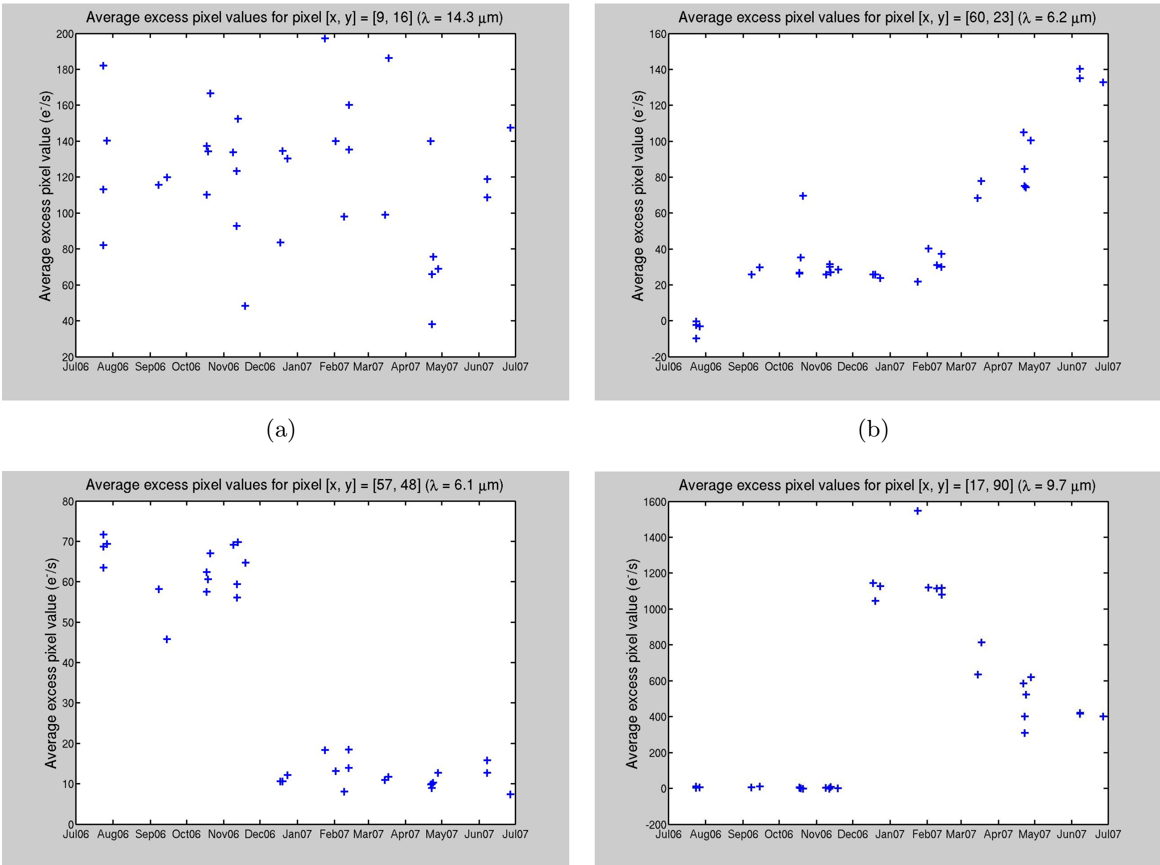

(a) (b) (c) (d)

Figure 19: The excess pixel values (with respect to surrounding pixels) are plotted for several pixels as a function of the observing date of stars in our sample. The pixel values are averaged over all exposures on each target. Panel (a) shows a normal random distribution, as would be expected for different targets. The other three panels show distinctive patterns indicating that the pixel has been affected. For example, in November 2006 the pixel in panel (d) that is responsible for the 9.7 μm peak is still normal, but after December it is (semi-) permanently hot. The pixel may for example have been inflicted by a cosmic ray.

4 Results and conclusions

In the previous chapters we have described in detail our sample of 33 λ Boötis stars. Our study involved a photometric as well as a spectroscopic analysis of Spitzer IRS observations.

We have first composed an infrared spectral atlas of the stars in the sample, including two offset positions probing the vicinity of the stars. One particular star, HD 110411, has been studied in more detail. First we determined the radius of the star on the basis of photometric data at visual wavelengths. This allowed us to determine the onset of the infrared excess. We estimated this excess to start at approximately 10 microns. This implies a grain size much smaller than 1 μm. This supports the theory for an interstellar nebula surrounding the star.

To be able to further distinguish between a circumstellar or interstellar origin of the infrared excess we have compared the observed spectral energy distribution (SED) with theoretical SEDs for a debris disk or a reflection nebula . Unique theoretical SED solutions were not possible: the solutions turned out to be degenerate in that the observed SED would allow solutions based on either a circumstellar or interstellar origin. Additional information on the nature of the infrared excess has been based on the search for PAH features in the infrared spectrum. No PAH features were found. We have also looked whether we could find any characteristic rotational and vibrational molecular lines such as H_2 and CO. This would yield welcome information on the nature of the surrounding medium. However, no evidence for such lines has been detected. A difficulty in the line analysis has been the presence of bad pixels and a follow-up analysis will check all features for their genuineness.

In summary, we have not been able to find strong evidence in favour of or against any of the suggested theoretical models of the λ Boötis phenomenon. A possible indication for the accretion theory is the onset at 10 micron of the infrared excess.

For the comparison with theoretical models we have to be aware of the limitations of the idealized model described in this study. While the idealized spherical model describes a good first order approximation, one may expect deviations under more realistic circumstances. Issues such as cloud geometry, dynamical timescales and the homogeneity of the cloud are some of the factors that may have a strong influence. Furthermore, the accretion pattern is sustained for a few million years after the star has exited the cloud. It is therefore not unlikely that a λ Boötis star is observed outside the cloud. So while no conclusive evidence has been found to support the selective accretion theory, no contradicting evidence has been found either.

For a more decisive analysis we would suggest the following improvements for a future study. First, the data should be cleaned with IRSCLEAN to get rid of instrumental artefacts. Another immediate follow-up is the extension of the analysis to all stars in the sample. It would be helpful to have information on additional offset positions, which may improve the spatial information on the circumstellar environment and provide a better test for the model. It might also be helpful to probe more molecular species at mid-infrared and far-infrared wavelengths. While always desirable, it is not immediately necessary to obtain the observations with a longer integration time to improve the signal-to-noise ratio.

λ Boötis stars provide an extremely useful probe of stellar evolution and the influence of the stellar surroundings. However, the available data at the moment have failed to provide conclusive evidence for one or another model.

5 Acknowledgements

This report would not have reached this stage without the large support and encouragement of several people. In particular, I would like to thank Inga Kamp for her inspiring supervision, never-ending patience, faith and optimism. Also I am grateful to Reynier Peletier for his confidence in my ability to finish this project and, at times, providing the necessary strong directions. The many friends with whom I shared room 134 turned it into a relaxing and pleasant working environment. The many conversations with my fellow student Keimpe Nevenzeel have kept me on the path towards the finish line. Over the years, the discussions with Bernard Jones shed new light on many issues. I would also like to thank Hens Buiter for keeping me on my feet and on Earth. And Rien for always being there.

References

[1] S. M. Andrievsky. On the possible origin of λ Boo stars. *A&A*, 321:838–840, May 1997.

[2] E. M. Burbidge and G. R. Burbidge. The Chemical Compositions of Five Stars which Show Some of the Characteristics of Population II. *ApJ*, 124:116, July 1956.

[3] F. Castelli and R. L. Kurucz. Ultraviolet spectra for lambda Boo (HD 125162) computed with H_2 opacities and Lyman-alpha H-H and H-H^+ opacities. *A&A*, 372:260–275, June 2001.

[4] F. Castelli and R. L. Kurucz. New Grids of ATLAS9 Model Atmospheres. *ArXiv Astrophysics e-prints*, May 2004.

[5] P. Charbonneau. Particle transport and the Lambda Bootis phenomenon. I - The diffusion/mass-loss model revisited. *ApJ*, 405:720–726, March 1993.

[6] A. Gáspár, K. Y. L. Su, G. H. Rieke, Z. Balog, I. Kamp, J. R. Martínez-Galarza, and K. Stapelfeldt. Modeling the Infrared Bow Shock at δ Velorum: Implications for Studies of Debris Disks and λ Boötis Stars. *ApJ*, 672:974–983, January 2008.

[7] R. O. Gray. The spectral classification of the Lambda Bootis stars. *AJ*, 95:220–228, January 1988.

[8] U. Heiter. The abundance pattern of lambda Bootis stars. *A&A*, 381:959–970, January 2002.

[9] U. Heiter, W. W. Weiss, and E. Paunzen. The accretion/diffusion theory for lambda Bootis stars in the light of spectroscopic data. *A&A*, 381:971–981, January 2002.

[10] M. Hoogerheijde. Radiative Processes, lecture notes, Univ. Leiden, 2007.

[11] J. R. Houck, T. L. Roellig, J. van Cleve, W. J. Forrest, T. Herter, C. R. Lawrence, K. Matthews, H. J. Reitsema, B. T. Soifer, D. M. Watson, D. Weedman, M. Huisjen, J. Troeltzsch, D. J. Barry, J. Bernard-Salas, C. E. Blacken, B. R. Brandl, V. Charmandaris, D. Devost, G. E. Gull, P. Hall, C. P. Henderson, S. J. U. Higdon, B. E. Pirger, J. Schoenwald, G. C. Sloan, K. I. Uchida, P. N. Appleton, L. Armus, M. J. Burgdorf, S. B. Fajardo-Acosta, C. J. Grillmair, J. G. Ingalls, P. W. Morris, and H. I. Teplitz. The Infrared Spectrograph (IRS) on the Spitzer Space Telescope. *ApJS*, 154:18–24, September 2004.

[12] I. Kamp and E. Paunzen. The λ Bootis phenomenon: interaction between a star and a diffuse interstellar cloud. *MNRAS*, 335:L45–L49, September 2002.

[13] R. L. Kurucz. Atlas: a Computer Program for Calculating Model Stellar Atmospheres. *SAO Special Report*, 309, February 1970.

[14] J. R. Martínez-Galarza, I. Kamp, K. Y. L. Su, A. Gáspár, G. Rieke, and E. E. Mamajek. Infrared Emission by Dust Around λ Bootis Stars: Debris Disks or Thermally Emitting Nebulae? *ApJ*, 694:165–173, March 2009.

[15] G. Michaud. Diffusion Processes in Peculiar a Stars. *ApJ*, 160:641, May 1970.

[16] G. Michaud and Y. Charland. Mass loss in A and F stars - The Lambda Bootis stars. *ApJ*, 311:326–334, December 1986.

[17] W. W. Morgan, P. C. Keenan, and E. Kellman. *An atlas of stellar spectra, with an outline of spectral classification.* 1943.

[18] E. Paunzen. The λ Bootis stars. In J. Zverko, J. Ziznovsky, S. J. Adelman, and W. W. Weiss, editors, *The A-Star Puzzle*, volume 224 of *IAU Symposium*, pages 443–450, December 2004.

[19] E. Paunzen, I. K. Iliev, I. Kamp, and I. S. Barzova. The status of Galactic field λ Bootis stars in the post-Hipparcos era. *MNRAS*, 336:1030–1042, November 2002.

[20] M. A. C. Perryman, L. Lindegren, J. Kovalevsky, E. Hoeg, U. Bastian, P. L. Bernacca, M. Crézé, F. Donati, M. Grenon, M. Grewing, F. van Leeuwen, H. van der Marel, F. Mignard, C. A. Murray, R. S. Le Poole, H. Schrijver, C. Turon, F. Arenou, M. Froeschlé, and C. S. Petersen. The HIPPARCOS Catalogue. *A&A*, 323:L49–L52, July 1997.

[21] G. B. Rybicki and A. P. Lightman. *Radiative Processes in Astrophysics.* June 1986.

[22] A. Slettebak. The Spectrum of 29 Cygni. *ApJ*, 115:575, May 1952.

[23] A. Slettebak. The Spectra and Rotational Velocities of the Bright Stars of Draper Types B8-A2. *ApJ*, 119:146, January 1954.

[24] J. D. T. Smith, B. T. Draine, D. A. Dale, J. Moustakas, R. C. Kennicutt, Jr., G. Helou, L. Armus, H. Roussel, K. Sheth, G. J. Bendo, B. A. Buckalew, D. Calzetti, C. W. Engelbracht, K. D. Gordon, D. J. Hollenbach, A. Li, S. Malhotra, E. J. Murphy, and F. Walter. The Mid-Infrared Spectrum of Star-forming Galaxies: Global Properties of Polycyclic Aromatic Hydrocarbon Emission. *ApJ*, 656:770–791, February 2007.

[25] A. G. G. M. Tielens. Interstellar Polycyclic Aromatic Hydrocarbon Molecules. *ARAA*, 46:289–337, September 2008.

[26] K. A. Venn and D. L. Lambert. The chemical composition of three Lambda Bootis stars. *ApJ*, 363:234–244, November 1990.

[27] M. W. Werner, T. L. Roellig, F. J. Low, G. H. Rieke, M. Rieke, W. F. Hoffmann, E. Young, J. R. Houck, B. Brandl, G. G. Fazio, J. L. Hora, R. D. Gehrz, G. Helou, B. T. Soifer, J. Stauffer, J. Keene, P. Eisenhardt, D. Gallagher, T. N. Gautier, W. Irace, C. R. Lawrence, L. Simmons, J. E. Van Cleve, M. Jura, E. L. Wright,

and D. P. Cruikshank. The Spitzer Space Telescope Mission. *ApJS*, 154:1–9, September 2004.

[28] Wikipedia. Bootes — Wikipedia, the free encyclopedia, 2012. [Online; accessed 19-June-2012].